

Modeling of Ornithopter Flight Dynamics for State Estimation and Control

Jared Grauer and James Hubbard Jr.

Abstract—Interest in flapping-wing aircraft is mounting as the demand for miniature unmanned aircraft proliferates into several sectors of society. Simple and accurate flight dynamics models are needed to develop control algorithms to autonomously perform the challenging missions envisioned for these vehicles. This work presents a complete nonlinear multibody model of the ornithopter flight dynamics, guided by flight tests and system identification results, and cast into a canonical form for nonlinear control. Simulations of trimmed flight and pitch rate damping are presented, showing promise for more advanced control algorithms.

I. INTRODUCTION

ORNITHOPTERS, miniature flapping-wing air vehicles mimicking avian flight gaits, are receiving growing interest from hobbyists, researchers, and mission planners as these vehicles continue to proliferate in both civilian and military sectors. It is envisioned that the agility, maneuverability, robustness, and contextual camouflage exhibited by these vehicles will fill a niche in the design space left void by conventional fixed-wing and rotary-wing vehicles, and result in a fully autonomous flight vehicle that integrates multi-mission capabilities such as long endurance outdoor flight, super-agile indoor flight, and precision perching.

Vital to the achievement of these goals is the development of a simple but accurate flight dynamics model, which constitutes a significant challenge. The motions seen in flight are fast, large amplitude, and highly coupled, requiring nonlinear multibody models. The flapping wings create unsteady, three dimensional, low Reynolds number flows that are difficult to model. Additionally the small vehicle size admits high gust sensitivity due to low inertia and necessitates the use of low quality MEMS-based sensors for flight measurements.

Despite these challenges, progress is being made towards an autonomous ornithopter. Several studies have shown that ornithopters of an appreciable size require multibody models [1], [2], [3], [4]. Computational fluid dynamics has illustrated fundamental flow physics in flapping-wing flight [5], [6] and simple blade element models have been used to capture measured trends [7], [8]. Control algorithms have also been studied, primarily designing optimal wing trajectories for insect-based articulated wings [9], [10]. Currently, however, there do not exist plant models suitable for designing the nonlinear control needed for achieving an autonomous ornithopter.

This paper presents such a plant model for a commercially available ornithopter. The vehicle platform is described in

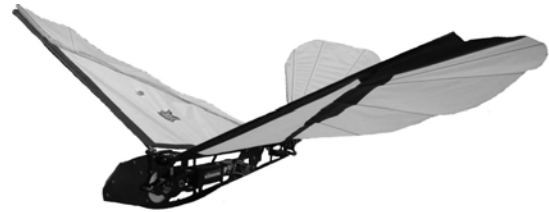


Fig. 1. Ornithopter test vehicle

Section II. In Section III-A the multibody dynamics are derived, and in Sections III-B and III-C actuator and aerodynamic models are determined using system identification. Simulation results for trimmed flight and pitch rate damping control are presented in Section IV, and a discussion of results is given in Section V.

II. ORNITHOPTER RESEARCH PLATFORM

The modeling work described herein was investigated using an experimental flapping-wing research platform, shown in Figure 1. This battery-powered “Slow Hawk” Kinkadee ornithopter was selected due to adequate flight performance, ease of piloting, robustness to weather and hard landings, and the ability to carry useful sensor payloads.

The ornithopter fuselage is machined from a single 3 mm ply of carbon fiber and houses the onboard electrical components. The wings are rip-stop polyester membrane sails, held together using dacron tape, a 5 mm carbon fiber spar running the leading edge, and a 3 mm carbon fiber spar running from the aft portion of the wing to the wing tip. The wings have a 1.2 m span, 0.4 m depth, 0.3 m² area, and a 4.4:1 aspect ratio. Similarly, the tail is a membrane with carbon fiber rods running from fore to aft along the centerline. The tail has 0.2 m span, 0.2 m length, 0.04 m² area, and 1.5:1 aspect ratio. The ornithopter has 0.446 kg total mass.

The ornithopter is flown in a similar manner as other hobby aircraft: a pilot launches the vehicle and then uses standard radio equipment to relay pilot joystick commands to an onboard receiver, which directs power from a lithium polymer battery to the actuators. The pilot throttle commands the speed of a Feigao DC motor, which through a gearbox and a four-bar linkage, flaps the wing to generate thrust and lift forces. The pilot elevator and aileron joysticks command two Hitec HS-56 servo motors that are aligned in a serial fashion to pitch and roll the tail relative to the fuselage, creating aerodynamic pitching and yawing control torques. This ornithopter flaps up to 8 Hz, flies up to 10 m/s, and

The authors are with the Morpheus Laboratory, University of Maryland, College Park, MD 20742.

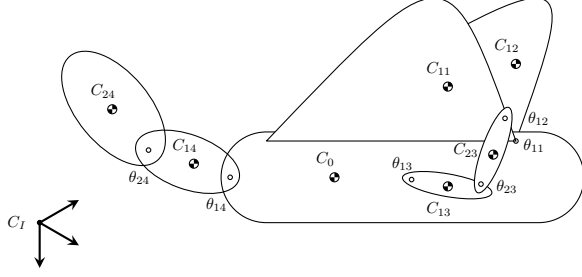


Fig. 2. Multibody ornithopter assembly

experiences Reynolds numbers between 19,000 and 232,000 along its wings.

III. FLIGHT DYNAMICS MODEL

A. Rigid Body Dynamics

Dynamics of conventional aircraft are typically well-approximated with those of a single rigid body. Recent flight tests however have reported that this ornithopter, flapping at 4.69 Hz, experiences 5.62 rad/s pitch rates and 46.11 m/s² heave accelerations in trimmed straight and level mean flight [1], requiring multibody models to capture. Additional modeling efforts have shown that the flapping wings significantly alter the center of mass position and elements of the inertia tensor [2], supporting the case for a multibody model.

Many methods and computer tools exist for generating equations of motion for multibody systems in a variety of formats. Here, the ornithopter equations were derived analytically using Lagrangian dynamics. This method is procedural to implement, uses the minimal number of state variables, and directly forms ordinary differential equations. Additionally the equations of motion can be cast into canonical forms for nonlinear control, for which the energy expressions provide inspiration for Lyapunov control functions.

The ornithopter multibody model is shown in Figure 2 and consists of seven rigid bodies: the fuselage, two wings, the four-bar crank and coupler, the tail mounting piece, and the tail. The four-bar crank and coupler were included in the model to reduce the dimension of the state vector and to form equations affine in the control input. Although flight data has reported evidence of structural modes in the fuselage, experiments and simulation studies have shown that rigid body approximations capture the trends measured in flight data [1], [2], [11]. Each rigid body has mass m_{ij} and inertia tensor \mathbf{I}_{ij} , where i and j refer to the linkage and chain indexes. Each body has also a coordinate frame $K_{ij} = \{\mathbf{e}_{xij}, \mathbf{e}_{yij}, \mathbf{e}_{zij}\}$ coincident with the center of mass C_{ij} . An inertial frame is taken at a point on the ground C_I , with primary axes pointing north, east, and down.

State variables were chosen to parallel standard aircraft and robot manipulator conventions. The generalized position of the ornithopter is

$$\mathbf{p} = [\mathbf{r}^T \quad \boldsymbol{\eta}^T \quad \boldsymbol{\theta}^T]^T \in \mathbb{R}^{N_p} \quad (1)$$

where \mathbf{r} is the inertial position of the fuselage center of mass; $\boldsymbol{\eta}$ is a quaternion describing the orientation of the fuselage, having vector part $\boldsymbol{\epsilon}$ and scalar part δ ; and $\boldsymbol{\theta}$ is a vector concatenating the four-bar crank angle θ_{13} , the tail pitch deflection θ_{14} and the tail roll deflection θ_{24} . The four-bar crank angle was chosen to describe the four-bar mechanism because numerical integration problems were incurred with parametrization using the wing angle.

The generalized velocity states are

$$\mathbf{v} = [\boldsymbol{\nu}^T \quad \boldsymbol{\omega}^T \quad \dot{\boldsymbol{\theta}}^T]^T \in \mathbb{R}^{N_v} \quad (2)$$

where $\boldsymbol{\nu}$ and $\boldsymbol{\omega}$ are the body-fixed translational and rotational velocities of the fuselage, and where $\dot{\boldsymbol{\theta}}$ is a vector of joint rates. The kinematic equations describing the evolution of the position states are

$$\dot{\mathbf{p}} = \mathbf{J}_K \mathbf{v} \quad (3)$$

where the kinematic Jacobian matrix \mathbf{J}_K has along its block-diagonal a rotation matrix

$$\mathbf{R}^{I,0} = (\delta^2 - \boldsymbol{\epsilon}^T \boldsymbol{\epsilon}) \mathbb{I} + 2\boldsymbol{\epsilon} \boldsymbol{\epsilon}^T + 2\delta S(\boldsymbol{\epsilon}) \quad (4)$$

a rotational Jacobian matrix

$$\mathbf{J}_\eta = \frac{1}{2} \begin{bmatrix} \delta \mathbb{I} + S(\boldsymbol{\epsilon}) \\ -\boldsymbol{\epsilon}^T \end{bmatrix} \quad (5)$$

and an identity matrix \mathbb{I} , where $S(\cdot)$ is a skew operator representing the cross-product operation.

A point p on rigid body ij with a distance \mathbf{r}_p from the center of mass, has absolute position, rotational velocity, and translational velocity

$$\mathbf{r}_p = \mathbf{r} + \mathbf{r}_{0j} + \sum_{k=1}^{i-1} (\mathbf{r}_{kj} - \mathbf{l}_{kj}) + (\mathbf{r}_p - \mathbf{l}_{ij}) \quad (6)$$

$$\boldsymbol{\omega}_p = \boldsymbol{\omega} + \mathbf{Z}_{ij} \dot{\boldsymbol{\theta}} \quad (7)$$

$$\boldsymbol{\nu}_p = \boldsymbol{\nu} + S(\boldsymbol{\omega}) \mathbf{r}_{0j} + \sum_{k=1}^{i-1} S(\boldsymbol{\omega}_{kj}) (\mathbf{r}_{kj} - \mathbf{l}_{kj}) + S(\boldsymbol{\omega}_{ij}) (\mathbf{r}_p - \mathbf{l}_{ij}) \quad (8)$$

respectively, where \mathbf{r}_{ij} and \mathbf{l}_{ij} are position vectors indicating the outboard and inboard joint locations from the center of mass, and where \mathbf{Z}_{ij} is a matrix of joint rotation axes.

Using (6) - (8) for the body centers of mass, the kinetic and potential energies of the system are

$$T(\mathbf{p}, \mathbf{v}) = \frac{1}{2} \sum_{i=0}^{N_{b,j}} \sum_{j=0}^{N_c} m_{ij} \boldsymbol{\nu}_{ij}^T \boldsymbol{\nu}_{ij} + \boldsymbol{\omega}_{ij}^T \mathbf{I}_{ij} \boldsymbol{\omega}_{ij} \quad (9)$$

$$U(\mathbf{p}) = - \sum_{i=0}^{N_{b,j}} \sum_{j=0}^{N_c} m_{ij} \mathbf{g}^T \mathbf{r}_{ij} \quad (10)$$

where N_c is the number of rigid body chains, $N_{b,j}$ is the number of rigid bodies on chain j , and \mathbf{g} is the acceleration due to gravity.

The dynamic equations of motion were derived using the Boltzmann-Hamel equations, which are a generalization of the Lagrange equations that account for position and velocity

state variables expressed in different coordinate frames. In matrix form, these equations are

$$\frac{d}{dt} \left[\frac{\partial T}{\partial \mathbf{v}} \right]^T + \left(\sum_{k=1}^{N_v} \frac{\partial T}{\partial v_k} \mathbf{\Gamma}_k \right) \mathbf{v} - \mathbf{J}_K^T \left[\frac{\partial T}{\partial \mathbf{p}} \right]^T = \boldsymbol{\tau} \quad (11)$$

where $\boldsymbol{\tau}$ is a vector of generalized exogenous forces and where $\mathbf{\Gamma}_k$ are Hamel coefficient matrices, given by

$$\mathbf{\Gamma}_k = \mathbf{J}_K^T \mathbf{\Lambda}_k \mathbf{J}_K \quad (12)$$

$$\{\mathbf{\Lambda}_k\}_{m,n} = \frac{\partial}{\partial p_n} \{\mathbf{J}_K\}_{k,m} - \frac{\partial}{\partial p_m} \{\mathbf{J}_K^T\}_{k,n}. \quad (13)$$

After some algebraic manipulation, the vehicle dynamics are cast in the canonical form

$$\mathbf{M}_b(\mathbf{p})\dot{\mathbf{v}} + \mathbf{C}_b(\mathbf{p}, \mathbf{v})\mathbf{v} + \mathbf{E}_b(\mathbf{p}, \mathbf{v}) = \boldsymbol{\tau} \quad (14)$$

where \mathbf{M}_b describes the generalized mass of the system, \mathbf{C}_b contains nonlinear forces arising from Coriolis and centripetal accelerations, and \mathbf{E}_b describes forces imparted on the system by the environment through which it moves, comprising aerodynamic $\mathbf{a}(\mathbf{p}, \mathbf{v})$ and gravitational $\mathbf{g}(\mathbf{p})$ contributions.

The mass matrix is symmetric, positive definite, and most easily found using algebraic substitutions to manipulate the kinetic energy in (9) into the quadratic form

$$T(\mathbf{p}, \mathbf{v}) = \frac{1}{2} \mathbf{v}^T \mathbf{M}_b \mathbf{v}. \quad (15)$$

The coupling matrix \mathbf{C}_b does not have a unique representation; however, by extension of Lewis [12], the representation

$$\begin{aligned} \mathbf{C}_b(\mathbf{p}, \mathbf{v}) = & \frac{1}{2} \dot{\mathbf{M}}_b + \sum_{k=1}^{N_v} \frac{\partial T}{\partial v_k} \mathbf{\Gamma}_k + \frac{1}{2} \left[\frac{\partial \mathbf{M}_b}{\partial \mathbf{p}} \right] (\mathbf{v} \otimes \mathbb{I}) \mathbf{J}_K \\ & - \frac{1}{2} \mathbf{J}_K^T (\mathbb{I} \otimes \mathbf{v}^T) \left[\frac{\partial \mathbf{M}_b}{\partial \mathbf{p}} \right]^T \end{aligned} \quad (16)$$

guarantees properties used in passivity control, where \otimes denotes the Kronecker product operator. The generalized force due to gravitational acceleration is

$$\mathbf{g}(\mathbf{p}) = \mathbf{J}_K^T \left[\frac{\partial U}{\partial \mathbf{p}} \right]^T. \quad (17)$$

B. Actuator Dynamics

The pilot throttle, tail pitch angle, and tail roll angle joystick inputs

$$\mathbf{u} = [u_{thr} \quad u_{lon} \quad u_{lat}]^T \quad (18)$$

are transmitted to onboard actuators that apply torques $\boldsymbol{\tau}$ to the articulated joint angles. Inclusion of actuator dynamics captures additional inertia, damping, and stiffness, improving simulation fidelity and increasing accuracy of parameter estimates identified from flight data, thus providing control laws with more accurate plant models. Additionally control laws can be directly implemented in hardware and include saturation limits.

TABLE I
ESTIMATED ACTUATOR MODEL PARAMETERS

	ϕ	$\dot{\phi}$	$s(\hat{\phi})$
DC Motor	M_a	$+2.2074 \times 10^{-4}$	1.0835×10^{-5}
	C_a	$+1.0069 \times 10^{-3}$	4.6541×10^{-5}
	B	$-6.3158 \times 10^{+1}$	1.0164×10^{-2}
	$G_{a,13}$	1.8651	—
Servo Motor	M_a	$+2.6291 \times 10^{-5}$	1.1243×10^{-5}
	C_a	$+6.4933 \times 10^{-4}$	2.5415×10^{-4}
	B	-8.8359×10^{-3}	3.4789×10^{-3}
	$G_{a,14}$	6.25	—
	$G_{a,24}$	1	—

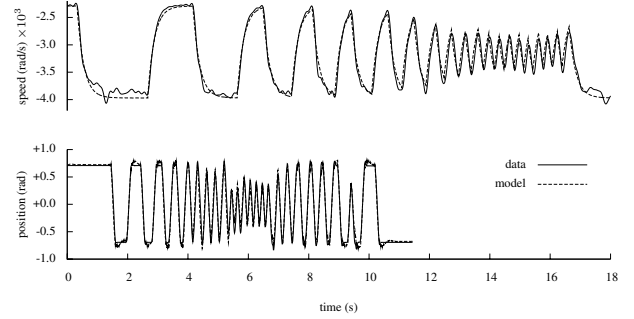


Fig. 3. DC motor and servo motor model fits using output-error

The onboard DC motor and servo motor actuators were modeled as

$$\mathbf{M}_a \dot{\mathbf{v}} + \mathbf{C}_a \mathbf{v} + \mathbf{G}_a \boldsymbol{\tau} + \mathbf{K}_a \mathbf{p} = \mathbf{B} \mathbf{u} \quad (19)$$

where \mathbf{M}_a describes the armature rotary inertia; \mathbf{C}_a describes damping terms arising from viscous friction, back electro-mechanical force, electrical resistance, and current/torque coupling; \mathbf{G}_a is a matrix of gear ratio parameters, \mathbf{K}_a captures the synthetic stiffness created by the proportional feedback in the servo motors, and \mathbf{B} is a control effectiveness matrix.

An experiment was performed where the actuators were subject to a series of step inputs while measuring reaction torque, angular position, and angular velocity [13]. Parameter estimates $\hat{\phi}$ and color-corrected standard errors $s(\hat{\phi})$ presented in Table I were determined using a combined equation-error/output-error approach [14]. Servo motor stiffness have the opposite sign of the control effectiveness coefficients. Gear ratios $G_{a,ij}$ were measured and not estimated. The model fit the data well, and output-error results are shown in Figure 3, where the coefficients of determination were 0.98 for both the DC motor and the servo motor.

Substituting the rigid body dynamics (14) into the actuator dynamics (19) and rearranging yields

$$\mathbf{M} \dot{\mathbf{v}} + \mathbf{C} \mathbf{v} + \mathbf{E} = \mathbf{B} \mathbf{u} \quad (20)$$

where \mathbf{M} absorbs the system inertia, \mathbf{C} absorbs the coupling accelerations and the damping, and \mathbf{E} absorbs the gravitational, aerodynamic, and feedback forces.

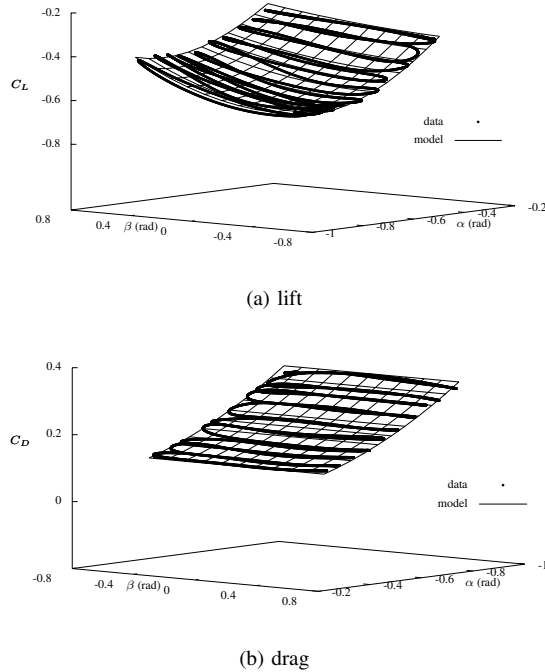


Fig. 4. Tail aerodynamic coefficient model fits

C. Aerodynamics

The lifting bodies of the ornithopter were assumed to be only the two wings and tail, and their effects independent of one another. Steady aerodynamic models for the tail were identified from wind tunnel tests in flows up to 10 m/s. Modified step-wise regression [14] was employed to determine the model structure

$$C_L = C_{L_0} + C_{L_\alpha} \alpha + C_{L_{\alpha\beta}} \alpha \beta + C_{L_{\alpha^3}} \alpha^3 + C_{L_{\alpha^2\beta^2}} \alpha^2 \beta^2 \quad (21)$$

$$C_D = C_{D_0} + C_{D_{\alpha^2}} \alpha^2 \quad (22)$$

for the lift and drag force coefficients from force balance data, where α is the angle of attack and β is the sideslip angle. The equation-error method [14] was used to estimate model parameters, which are given in Table II. Model fits had coefficients of determination 0.98 for lift and 0.99 for drag, and are illustrated as response surfaces in Figure 4.

A flight test was conducted to determine an aerodynamic model for the wings from flight test data, details of which can be found in [11]. Solving for the aerodynamic effects in (20) and substituting state measurements facilitates the system identification of the aerodynamic forces. A common model for the lift and drag force coefficients of flapping wings is the quasi-steady model

$$C_L = C_{L_0} + C_{L_\alpha} \alpha + C_{L_{\dot{\alpha}}} \dot{\alpha} + C_{L_{\dot{h}}} \dot{h} \quad (23)$$

$$C_D = C_{D_0} + C_{D_\alpha} \alpha + C_{D_{\alpha^2}} \alpha^2 \quad (24)$$

where \dot{h} is a wind-frame plunging velocity and where all aerodynamic variables are referenced to the wing mean aerodynamic chord. The lift model includes a steady lift

TABLE II
ESTIMATED AERODYNAMIC MODEL PARAMETERS

	ϕ	$\hat{\phi}$	$s(\hat{\phi})$
Tail	C_{L_0}	+0.1219	0.0227
	C_{L_α}	+1.1996	0.0566
	$C_{L_{\alpha\beta}}$	-0.1874	0.0130
	$C_{L_{\alpha^3}}$	-0.5409	0.0466
	$C_{L_{\alpha^2\beta^2}}$	+0.2657	0.0341
	C_{D_0}	+0.0784	0.0034
	$C_{D_{\alpha^2}}$	+0.3404	0.0080
Wings	C_{L_0}	-0.6044	0.1528
	C_{L_α}	+1.1516	0.1987
	$C_{L_{\dot{\alpha}}}$	+0.0448	0.0029
	$C_{L_{\dot{h}}}$	+0.1079	0.0187
	C_{D_0}	-0.0612	0.0160
	C_{D_α}	+0.1544	0.0237
	$C_{D_{\alpha^2}}$	-1.0946	0.0893

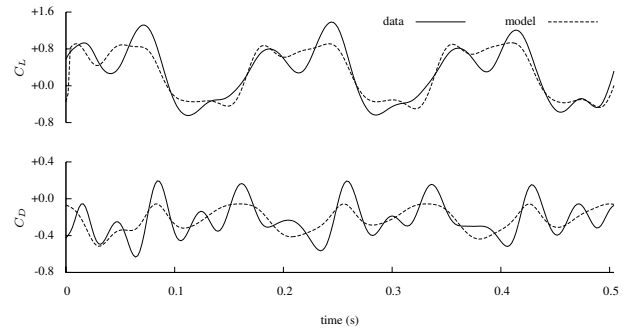


Fig. 5. Wing aerodynamic coefficient model fits

component, as well as contributions from pitching and plunging. The drag model includes a bias term reflecting steady thrust and drag, and a quadratic series in angle of attack that captures both the drag polar and the 2/flap thrust contributions. Parameters were estimated using the equation-error method and are given in Table II. The model captured the main trends in the flight data, shown in Figure 5 and having coefficients of determination 0.81 for lift and 0.43 for thrust.

The aerodynamic force acting on the lifting body ij is

$$\tau_{a,ij} = QS \begin{bmatrix} \sin \alpha & -\cos \alpha \cos \beta \\ 0 & \sin \beta \\ -\cos \alpha & -\sin \alpha \cos \beta \end{bmatrix} \begin{bmatrix} C_L \\ C_D \end{bmatrix} \quad (25)$$

where Q is the dynamic pressure at the mean aerodynamic center and S is the reference area. The generalized aerodynamic forces are then

$$\mathbf{a}(\mathbf{p}, \mathbf{v}) = - \sum_{i=0}^{N_{b,j}} \sum_{j=0}^{N_c} \mathbf{J}_{a,ij} \tau_{a,ij} \quad (26)$$

where $\mathbf{J}_{a,ij}$ is a Jacobian matrix transforming a point force on body ij into generalized forces on the system.

A block diagram summarizing the ornithopter dynamics is illustrated in Figure 6. The pilot inputs \mathbf{u} are transmitted to the ornithopter radio equipment, where they are parsed to the actuators, which generate control torques τ on the aircraft joint angles. Gravitational and aerodynamic forces also act

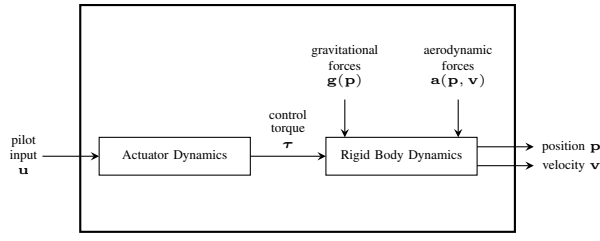


Fig. 6. Ornithopter model block diagram

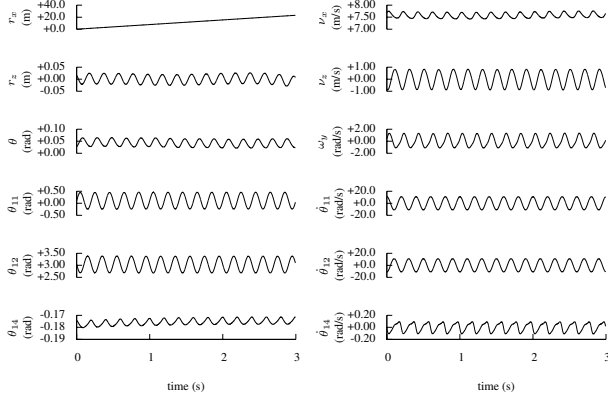


Fig. 8. Longitudinal state trajectories in straight and level mean flight

on the rigid body dynamics, evolving position \mathbf{p} and velocity \mathbf{v} states through time.

IV. SIMULATION RESULTS

This section presents computer simulations of the presented flight dynamics. The equations of motion given by (3) and (20) describe nineteen ordinary differential equations that were solved numerically in MATLAB using the implicit solver `ode15s`.

A. Trimmed Straight and Level Mean Flight

The ornithopter was trimmed for straight and level mean flight. A trim state of the aircraft was heuristically found to have a mean flight velocity 7.79 m/s and 0.06 rad angle of attack. The control states were picked to flap the ornithopter at 5.8 Hz with -0.17 rad pitch and 0.00 rad roll deflection of the tail.

A series of silhouettes illustrating the flight trajectory and vehicle configuration are shown in Figure 7, taken at 0.125 s intervals. Longitudinal position states and their corresponding velocities are shown in the columns of Figure 8. The ornithopter flew forward with a longitudinal velocity oscillating with 0.17 m/s and 0.86 m/s oscillations about the mean in the longitudinal and heave directions. Heave velocities translated into a 0.03 m oscillation in altitude. The Euler pitch angle θ exhibited a 0.04 rad oscillation about trim, and the pitch rate was 1.23 rad/s in amplitude. The longitudinal tail experienced small oscillations arising from the aerodynamic loads and reaction forces at the joint angles.

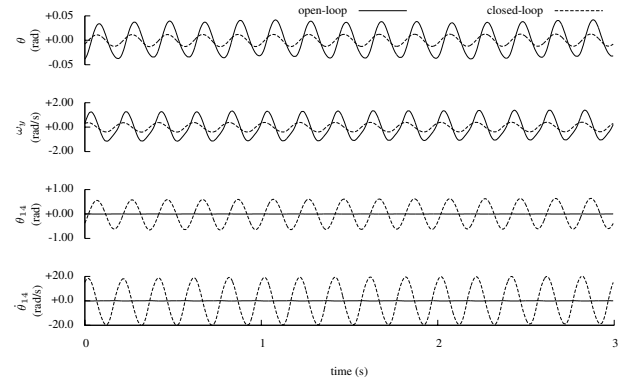


Fig. 9. Effect of pitch rate feedback on perturbations from trim

B. Pitch Rate Damping

One application for ornithopters is serving as an autonomous aerial surveillance platform. The fast and large amplitude flight exhibited by the ornithopter research platform has resulted in poor quality video data and has required frequent replacement of onboard electronics. One simple approach for attenuating these vibrations is to feed back the fuselage pitch rate, as measured by an onboard MEMS gyroscope, to the longitudinal tail deflection. The control input for the longitudinal control would then be the summation of the pilot input and the feedback contributions

$$u_{lon} = u_{lon}^* + k_p \omega_y \quad (27)$$

where u_{lon}^* represents the pilot controls and k_p is a positive proportional gain.

The feedback control was applied to the ornithopter in simulation and results are shown in Figure 9 for the perturbations about the trimmed flight solution. The feedback gain was chosen so that the tail had a maximum deflection of 0.6 rad from trim. The control had the effect of reducing the pitch oscillation amplitude from 0.13 rad to 0.06 rad, and the pitch rate oscillation from 1.40 rad/s to 0.40 rad/s. These perturbations were decreased by more than a factor of two and significantly dampen the vibration to onboard visual and avionics equipment.

V. DISCUSSION AND FUTURE WORK

Ornithopters are flapping-wing vehicles which have the potential to exploit super agile and highly maneuverable flight at low speeds to accomplish a variety of mission profiles. However, obtaining a simple but accurate model of the flight dynamics models requisite for autopilot design and autonomous operation is a challenging task. This paper presents the development of a relatively low-dimension state-space model describing ornithopter flight dynamics, guided by flight tests, avionics measurements, analytical modeling, and system identification.

The ornithopter was modeled as a system of seven rigid bodies. This assumption ignores the structural deformations in the ornithopter but is able to capture the reaction forces and varying mass distribution caused by the flapping wings.

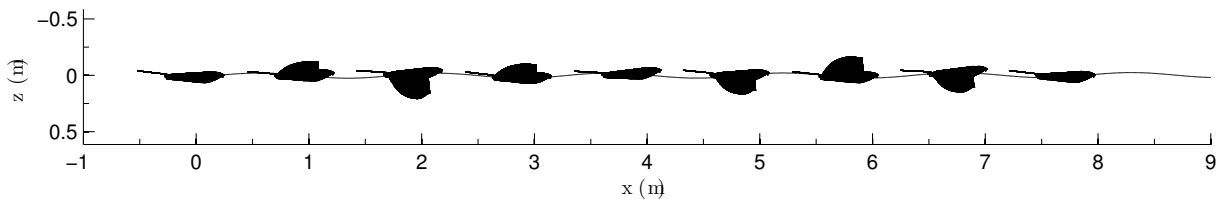


Fig. 7. Straight and level mean flight path and silhouettes in 0.125 s intervals

The equations of motion were derived using the Boltzmann-Hamel equations and cast in a form convenient for system identification and nonlinear control. System identification tools were used to obtain good actuator models using second order equations, which were then coupled with the rigid body equations. Tail aerodynamics were identified from wind tunnel tests, and system identification was again used, leveraging the ornithopter model, to identify a reasonable quasi-steady model of the wing aerodynamics.

Simulation studies were conducted to illustrate the ornithopter dynamics model. A trimmed solution for straight and level mean flight was presented, and a simple pitch rate damper was added to attenuate fuselage pitching motions for camera stabilization and vibration damping.

This paper presented a complete nonlinear multibody model of the ornithopter flight dynamics. The model was cast in a form convenient for nonlinear control. Future work centers around applying the under-actuated, nonlinear control strategies to this model needed for highly agile and maneuverable flight in confined and cluttered environments. Additionally state estimation routines will be implemented with typical sensors used on miniature aircraft. Although a quasi-steady aerodynamics model was presented, current work is underway to identify a more accurate model for the wing aerodynamics.

VI. ACKNOWLEDGMENTS

The authors wish to acknowledge the University of Maryland, the National Institute of Aerospace, and the NASA Langley Research Center for their support in this research. Funding was supplied by the Army MAST Collaborative Technology Alliance. The authors would additionally like to thank the members of the Morpheus Laboratory and Autonomous Vehicle Laboratory for their continued teamwork and motivation.

REFERENCES

- [1] J. Grauer and J. Hubbard, "Inertial measurements from flight data of a flapping-wing ornithopter", *Journal of Guidance, Control, and Dynamics*, vol. 32, no. 1, pp. 326–331, January-February 2009.
- [2] J. Grauer and J. Hubbard, "Multibody model of an ornithopter", *Journal of Guidance, Control, and Dynamics*, vol. 32, no. 5, pp. 1675–1679, September-October 2009.
- [3] M. Bolender, "Rigid multi-body equations-of-motion for flapping-wing mavs using kane's equations", Number AIAA-2009-6158.
- [4] T. Rashid, "The flight dynamics of a full-scale ornithopter", Master's thesis, University of Toronto, 1995.
- [5] M. Vest and J. Katz, "Unsteady aerodynamic model of flapping wings", *AIAA Journal*, vol. 34, no. 7, pp. 1435–1440, July 1996.
- [6] B. Roget, J. Sitaraman, R. Harmon, J. Grauer, J. Hubbard, and S. Humbert, "Computational study of flexible wing ornithopter flight", *Journal of Aircraft*, vol. 46, no. 6, pp. 2016–2031, November-December 2009.
- [7] S. Sane and M. Dickinson, "The aerodynamic effects of wing rotation and a revised quasi-steady model of flapping flight", *Journal of Experimental Biology*, vol. 205, no. 8, pp. 1087–1096, April 2002.
- [8] R. Harmon, J. Grauer, J. Hubbard, J. Conroy, J. Humbert, J. Sitaraman, and B. Roget, "Experimental determination of ornithopter membrane wing shapes used for simple aerodynamic modeling", Number AIAA-2008-6237.
- [9] X. Deng, L. Schenato, and S. Sastry, "Flapping flight for biomimetic robot insects: Part ii - flight control design", *IEEE Transactions on Robotics*, vol. 22, no. 4, pp. 789–803, August 2006.
- [10] D. Doman, M. Oppenheimer, and D. Sigthorsson, "Wingbeat shape modulation for flapping wing micro air vehicle control during hover", *Journal of Guidance, Control, and Dynamics*, 2010.
- [11] J. Grauer, E. Ulrich, J. Hubbard, D. Pines, and S. Humbert, "Model structure determination of an ornithopter aerodynamics model from flight data", 2010, number AIAA-2010-41.
- [12] F. Lewis, D. Dawson, and C. Abdallah, *Robot Manipulator Control: Theory and Practice*, CRC, 2004.
- [13] J. Grauer and J. Hubbard, "Identification and integration of ornithopter actuator models", 2009, number AIAA-2009-5937.
- [14] V. Klein and E. Morelli, *Aircraft System Identification*, AIAA, 2006.